Accepted Manuscript

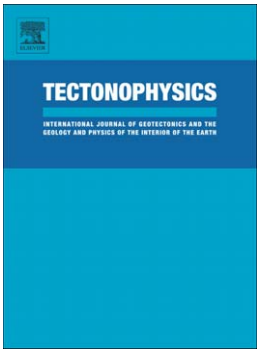

Lithospheric 3D gravity modelling using upper-mantle density constraints: Towards a characterization of the crustal configuration in the North Patagonian Massif area, Argentina

María Laura Gómez Dacal, Claudia Tocho, Eugenio Aragón, Judith Sippel, Magdalena Scheck-Wenderoth, Alexis Ponce

PII: S0040-1951(17)30057-4
DOI: doi:10.1016/j.tecto.2017.02.011
Reference: TECTO 127403

To appear in: *Tectonophysics*

Received date: 1 November 2016
Revised date: 8 February 2017
Accepted date: 13 February 2017

Please cite this article as: Dacal, María Laura Gómez, Tocho, Claudia, Aragón, Eugenio, Sippel, Judith, Scheck-Wenderoth, Magdalena, Ponce, Alexis, Lithospheric 3D gravity modelling using upper-mantle density constraints: Towards a characterization of the crustal configuration in the North Patagonian Massif area, Argentina, *Tectonophysics* (2017), doi:10.1016/j.tecto.2017.02.011

This is a PDF file of an unedited manuscript that has been accepted for publication. As a service to our customers we are providing this early version of the manuscript. The manuscript will undergo copyediting, typesetting, and review of the resulting proof before it is published in its final form. Please note that during the production process errors may be discovered which could affect the content, and all legal disclaimers that apply to the journal pertain.

ACCEPTED MANUSCRIPT

Lithospheric 3D gravity modelling using upper-mantle density constraints: towards a characterization of the crustal configuration in the North Patagonian Massif area, Argentina.

María Laura Gómez Dacal[a,b,*], Claudia Tocho[a,c], Eugenio Aragón[b,d], Judith Sippel[e], Magdalena Scheck-Wenderoth[e,f], Alexis Ponce[g]

[a] *Departamento de Gravimetría, Facultad de Ciencias Astronómicas y Geofísicas, Universidad Nacional de La Plata, Paseo del Bosque s/n, B1900FWA, La Plata, Buenos Aires, Argentina. Tel.: +54-0221-4236593. gomezdacal@fcaglp.unlp.edu.ar*

[b] *Consejo Nacional de Investigaciones Científicas y Técnicas, Av. Rivadavia nº 1917, C1033AAJ, Ciudad Autónoma de Buenos Aires, Argentina*

[c] *Comisión de Investigaciones Científicas de la Provincia de Buenos Aires. 526, 10 y 11. B1900FWA La Plata, Buenos Aires, Argentina.*

[d] *Facultad de Ciencias Naturales y Museo, Universidad Nacional de La Plata, Centro de Investigaciones Geológicas, 1 nº 644, B1900FWA, La Plata, Buenos Aires, Argentina.*

[e] *Section 6.1 Basin Modelling, Helmholtz Centre Potsdam, GFZ German Research Centre for Geosciences, Potsdam, Germany.*

[f] *Department of Geology, Geochemistry of Petroleum and Coal, RWTH Aachen University, Aachen, Germany.*

[g] *Instituto de Ciencias de la Tierra y Ambientales de La Pampa (CONICET- UNLPam), Av. Uruguay 151, 6300 Santa Rosa, La Pampa, Argentina.*

Abstract

The North Patagonian Massif is an Argentinean plateau that has an average height of 1200 m and stands from 500 to 700 m above the neighboring areas. During Paleogene, it suffered a sudden uplift of more than 1200 m without noticeable internal deformation; thus, it could be related to isostatic disequilibrium. To shed light on the geodynamic development of the area it is necessary to characterize the present-day configuration of the crust. In this study, a lithospheric-scale 3D density model was developed by integrating all the available data of the area with the objective of assessing the depth of the crust-mantle discontinuity (Moho). During the construction of the initial density model, we tested different mantle density scenarios obtained using P- and S-wave veloc-

*Corresponding author.

ACCEPTED MANUSCRIPT

ities from tomographic models, converting them into densities and comparing the conversions with densities obtained from xenoliths. Below the North Patagonian Massif plateau, we have derived a Moho depth between 40 and 50 km which is from 2 to 7 km deeper than its surroundings. There is an evident correlation between high topography and deep Moho that would indicate isostatic equilibrium at present. The model results provide a new approach to the Moho depth in an area where there is no seismic constraining information about this discontinuity. In addition, we found a spatial correlation between the variation of the mean crustal density and the location of the Paleozoic terranes that were proposed to constitute the basement of Argentina.

Keywords: 3D gravity modelling, crustal configuration, North Patagonian Massif, seismic tomography, xenoliths.

---

1. Introduction

The backarc of the southern Andes in North Patagonia, Argentina, ($36°S$ to $45°S$) is composed of a heterogeneous crust where there are many sedimentary basins of different origins that are surrounding the so-called North Patagonian Massif (NPM) plateau (Figure 1; Aragón et al. 2011 b). It is located 400 km east of the trench of the subduction margin that links the South American and the Nazca tectonic plates. It covers an area of 100000 km^2 and is framed by crustal morpho-structural lineaments called Limay, Gastre, Los Chacays and El Gualicho (Figure 1) that allow regional relative movements. Because of its height (about 1200 m above sea level), the NPM plateau is distinguished from the surrounding basins, called Neuquén, Colorado, Ñirihuau and Cañadon Asfalto, that are about 500 to 700 m lower in altitude than the plateau (Figure 1).

The present-day elevation of the NPM plateau was caused by a sudden uplift (Aragón et al., 2011 b) constrained by Paleocene (60 Ma) marine sediments and Oligocene (35 Ma) basalt flows that spilt from the top of the plateau (Aragón et al., 2010). Hence, the area was elevated more than 1200 meters after the

ACCEPTED MANUSCRIPT

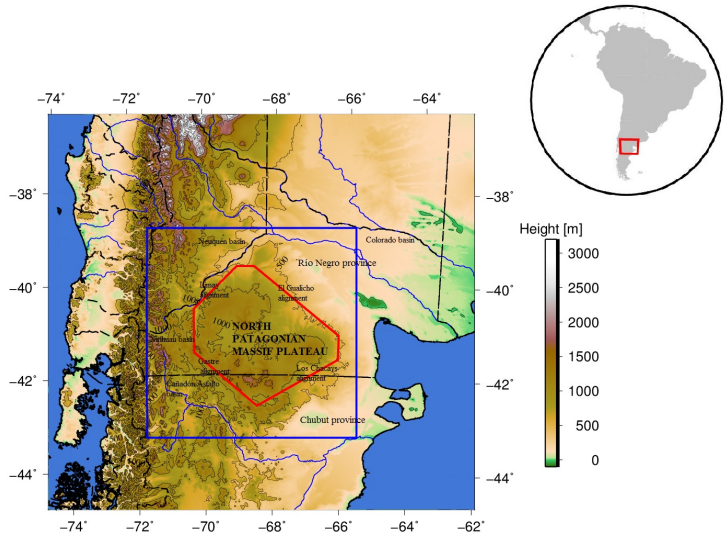

Figure 1: Topographic and geographic map of the backarc of North Patagonia, Argentina, including the modelled area, delimited in blue, and the location of the North Patagonian Massif plateau, in red.

Paleocene and before the late Oligocene basalts, and the tectonic inversion that built the neighboring Andes in the Miocene. There is no evidence of internal deformation in the NPM area during the mentioned uplift; the marine sediments from the Cretaceous-Tertiary boundary lay horizontally at 1100 m above sea level and they do not exhibit deformation inside the NPM plateau. By contrast, in the surrounding areas, these sediments are at a height between 300 and 500 m above sea level and they document different degrees of deformation associated with a Miocene phase of tectonic inversion (Aragón et al. 2010 and Aragón et al. 2011 a). Moreover, during the uplift time (Paleogene), a regional extensional system was developed in the area (rifting; Aragón et al. 2015), caused by the development of a slab window and mantle upwelling (Aragón et al., 2011 b). The described geological evidence lead to questions about the geodynamic processes that have generated the high elevation of the NPM plateau.

The NPM area behaved as an independent morpho-structural unit that experienced epeirogenic uplift (Aragón et al., 2011 a). These movements could

ACCEPTED MANUSCRIPT

have been generated by isostatic disequilibrium. Isostasy works toward an equilibrium state of the lithosphere in terms of vertical loads that thus become laterally equal at a certain depth of compensation. Hence, if a region is not isostatically balanced, buoyancy forces act and induce vertical movements to restore isostatic equilibrium. Nevertheless, before making statements about the geodynamic evolution of the NPM since pre-Oligocene times, it is necessary to understand its present-day physical state. Because the vertical loads depend on density, investigating the lithospheric-scale density configuration is essential to estimate the current isostatic state.

The main objective of this work is to assess the lithospheric density configuration of the North Patagonian Massif plateau and its surrounding areas (Figure 1) by using gravity modelling. As gravity analysis produces non-unique solutions, independent constraints need to be included. The major challenge of the area consists in the scarcity of seismic data that would illustrate the crustal discontinuities, but there are different seimological data for the mantle. Therefore, we emphasized the study in obtaining the mantle density configuration by analyzing the seismological data of tomographic models. The density configurations were constrained with independent density values derived from xenoliths to identify the more realistic one. Then, we integrated the selected configuration for the mantle with the other available data into a 3D gravity modelling procedure to assess the Moho depth and the density configuration of the crust.

2. Modelling approach

2.1. 3D Gravity modelling

The development of a gravity-constrained 3D density model requires setting up an initial model including all significant geological and geophysical observations. Subsequently, the free parameters of the initial model can be modified until the gravity calculated from the model fits with the measured gravity. For this purpose, we have used IGMAS+ software (Interactive Geophysical Modelling ASsistant, Götze & Schmidt 2010). IGMAS+ is an interactive software

ACCEPTED MANUSCRIPT

that allows to perform 3D gravity modelling by the use of triangulated grids that approximate different bodies, each with a constant density (Götze & Schmidt, 2010). The interfaces between modelled units are defined through a number of parallel vertical cross sections (working sections) and automatically triangulated by the software generating the three-dimensional bodies. Based on an initial 3D model, IGMAS+ allows to vary the model geometry and density interactively.

The initial model has an areal extension of 500 km x 500 km, including the NPM plateau and a surrounding area (Figure 1). The aim of the selection of the area is to compare the crustal configuration inside and outside the NPM plateau.

Figure 2(a) shows a profile of the 3D density model, including all considered data. It shows the initial model that consists of four bodies: sediments, two different crustal domains and mantle, the selected densities for each body as well as the constraining data, for the geometry of the discontinuities and for the densities, and the measured gravity used.

Bouguer anomalies from EGM2008 geopotential model (Earth Gravitational Model, Pavlis et al. 2012) have been used. EGM2008 has been released by the U.S. National Geospatial-Intelligence Agency (NGA) and is complete to spherical harmonic degree and order 2159. Figure 2(b) illustrates that there are negative Bouguer anomaly values inside the NPM plateau area, being all of them lower than -60 $mGal$ and reaching a minimum of -100 $mGal$ in the south-western parts of the plateau. These values are similar to the Bouguer anomaly values found in the mountain ranges of the Andes, where there are crustal roots (Lowrie, 2007). In the basins that surround the NPM, there are higher values measured increasing eastward from the Andes towards lower topography (Figure 2(b)). A correlation between topography (Figure 1) and Bouguer anomalies (Figure 2(b)) is evident: whenever a high topography is found the anomalies are low, this can be seen in the Andes as well as in the NPM. The opposite – high Bouguer anomaly values correlated with low relief areas – can be observed in the east of the modelled region where the Atlantic passive margin is located and to the north and south of the NPM.

ACCEPTED MANUSCRIPT

2.2. Constraints on the density configuration of the sediments

The discontinuity between the sediments and the upper crust (Figure 2(c)) was digitized from the Mobil isopaches of ICONS atlas (Heine, 2007), a compilation of data for intracontinental sedimentary basins world-wide. The south of Neuquén basin is the only area with sediment thicknesses larger than 200 m in the modelled domain (Figure 2(c)).

A constant density value (2400 kg/m^3) for the sediments was used because the sediment thicknesses are low (Figure 2(c)) and porosity (compaction) effects are expected to be minor. Including more detail would require more data and would not imply a significant improvement of a lithospheric scale model. The sediment density value was selected according to the different lithologies known to fill the Neuquén basin (Canale et al., 2015), because it is the area where the major volume of sediments can be found in the modelled zone.

2.3. Constraints on the density configuration of the crust

The initial shape for the Moho was extracted from a regional model of South America (Assumpção, personal communication) developed mainly on seismic data, such us point estimates from seismic refraction experiments, receiver functions analysis and surface wave dispersion (Assumpção et al., 2012). Gaps of seismic information have been filled with gravity-based estimates from Tassara & Echaurren (2012). The model has a resolution of 0.5° (Figure 2(d)). According to this model, the Moho depth beneath the NPM is between 32 and 38 km and it is surrounded by a thinner crust towards the north, east and north-west and by a thicker crust in the west. As the model lacks information in the south, we have interpolated between existing values to obtain an initial Moho surface for the model.

Even though the model of Assumpção et al. (2012) is based on a large database, there are only a few point estimates of Moho depth in the NPM area (Figure 2(d), Assumpção personal communication). These points, as they are gravity-independent Moho depth values from seismics, were used as control points of the final shape of the Moho in this study.

ACCEPTED MANUSCRIPT

Some constraints on crustal density could come from exposed crustal rocks described in geological studies. The studies in the area point out that the constituting sub-sedimentary crystalline crust of the NPM comprises early and late Paleozoic metamorphic complexes intruded by Ordovician, Devonian, Carboniferous, Permian, and Triassic plutonic rocks (Pankhurst et al., 2006), alternated by large Triassic and Jurassic volcanic rhyolitic complexes (Rapela et al., 2005), and overlain by thin Triassic and Jurassic sediments. These geologic units, in turn, were subject to strong erosion that developed, from late Jurassic to early Cretaceous times, an extended planation surface (flat topography) that was covered by a thin layer of upper Cretaceous (marine) and Tertiary (continental) sediments. Most of the south-eastern side of the Massif is covered by Oligocene plateau basalts that were erupted from the top of the massif onto the surrounding lower land (Aragón et al., 2011 b). To the north of the NPM plateau area, the basement is composed mostly by granites, granodiorites, rhyolites and andesitic to rhyolitic volcaniclastic successions (Gregori et al. 2008 and Kostadinoff et al. 2005). Even if Gregori et al. (2008) and Kostadinoff et al. (2005) suggest a possible connection between the rocks in the NPM and the basement to the north, they also mentioned that methamorphic rocks are more abundant in the NPM area, and thus the shallower crustal rocks can be slightly denser in the NPM than in the north.

For the deep crustal structure, the S-wave velocity model SL2013Sv of Schaeffer & Lebedev (2013) provides valuable information for the depth level at 25 km. The velocity distribution was converted to density in two steps: first P-wave velocities (V_p) have been calculated from the S-wave velocities (V_s) using,

$$V_p = 1.75 * V_s \tag{1}$$

The used factor is a value in the ranges described in several works for different areas in the world, such as Alvarado et al. (2007); Julià & Mejía (2004); Nakajima et al. (2001) among others. Nakajima et al. (2001) have found this value as the average for the lower-crust in northeastern Japan and in Alvarado

ACCEPTED MANUSCRIPT

et al. (2007) the value appears as the mid-range value for the northern part of Chilenia terrane. This constant factor allows us to obtain P-wave velocities that are similar to those expected for 25 km depth in ak135 model (Kennett et al., 1995).

The second step was to convert the obtained P-wave velocity distribution into densities (Figure 2(e)), which was done using a modification of Birch's law (Birch, 1961) that takes the form

$$\rho = aV_p + b \tag{2}$$

with ρ being the density, V_p the P-wave velocity and a and b constants depending on the lithology. We have used a different "b" factor that fits with the densities obtained from lower crust xenoliths. They are granulites enclosed in Paleogene basalts from Paso de los Indios, unique location where we have lower crust xenoliths data (locality V, Figure 2(b)). The mentioned xenoliths are described in the work of Castro et al. (2011). Their densities were calculated using the whole-rock analyses of major elements (Castro et al., 2011) and the CIPW norm (Johannsen, 1931) to reconstruct the minerals that might have composed the original rock (without the alterations caused by temperature, pressure or other effects) and their proportions. Using these density constraints, the modified Birch's law applied was

$$\rho = 0.3788V_p + 0.33 \tag{3}$$

The final density configuration for 25 km is shown in Figure 2(e), where a clear tendency in the density values can be observed from lower densities in the north-west to higher densities in the south-east.

Ramos (1988) has proposed the existence of different terranes forming the crystalline crustal basement of Argentina and Chile. These blocks are thought to have travelled long distances, before colliding with the south-west of Gondwana, during Proterozoic to Paleozoic times (Ramos, 1994). The modelled area is occupied mainly by two terranes, the southernmost part of Chilenia and the

ACCEPTED MANUSCRIPT

northern extreme of Patagonia (Figure 2(e)). Chilenia is suposed to have collided with Gondwana in Devonian times (Ramos, 1988) and it was the last of a sequence of collisions in central Argentina. Patagonia was proposed as an allochthonous terrane (Ramos, 1988) that might have collided with Gondwana in late Carboniferous times generating a subduction dipping south-west beneath the NPM (Vaughan & Pankhurst, 2008). Recent studies also point out the allochthonous character of Patagonia in a different way; they show that the Patagonia terrane is a piece of the Antartica Ross Orogen transported along the south-western Gondwana margin (Gonzalez et al. 2010, 2011a and Gonzalez et al. 2011b).

The sutures (terrane boundaries) between these blocks are major crustal discontinuities (Ramos, 1994) of which those in the study area, proposed by Chernicoff & Zappettini (2004) and based on magnetic data, are shown in Figure 2(e). The suture between Chilenia and Patagonia, derived from geological surface observations, largely coincides with the changing pattern of densities at 25 km depth (Figure 2(e)). Accordingly, Chilenia would have lower crustal density than Patagonia at this depth level. The contour levels of density are not fully coincident with the suture between Chilenia and Patagonia (Figure 2(e)), but they can express the limit between both areas at this depth. By following the surface expression of the limits between terranes, as shown on the map of Figure 2(e), we have divided the crust in two different bodies: Chilenia with a density of 2700 kg/m^3 and Patagonia with 2810 kg/m^3 (Figure 2(a)). The final densities chosen for the two bodies of crust are representative of values in the shallower and deeper rocks and a result of the combination of the previously exposed data.

2.4. Seismological constraints on the density configuration of the mantle

To obtain the density configuration in the upper mantle, two different tomographic models have been explored, one S-wave velocity model (Schaeffer & Lebedev 2013, Figure 2(a)) and one P-wave velocity model (Amaru, 2007).

The S-wave velocity model is called SL2013sv (Schaeffer & Lebedev, 2013)

ACCEPTED MANUSCRIPT

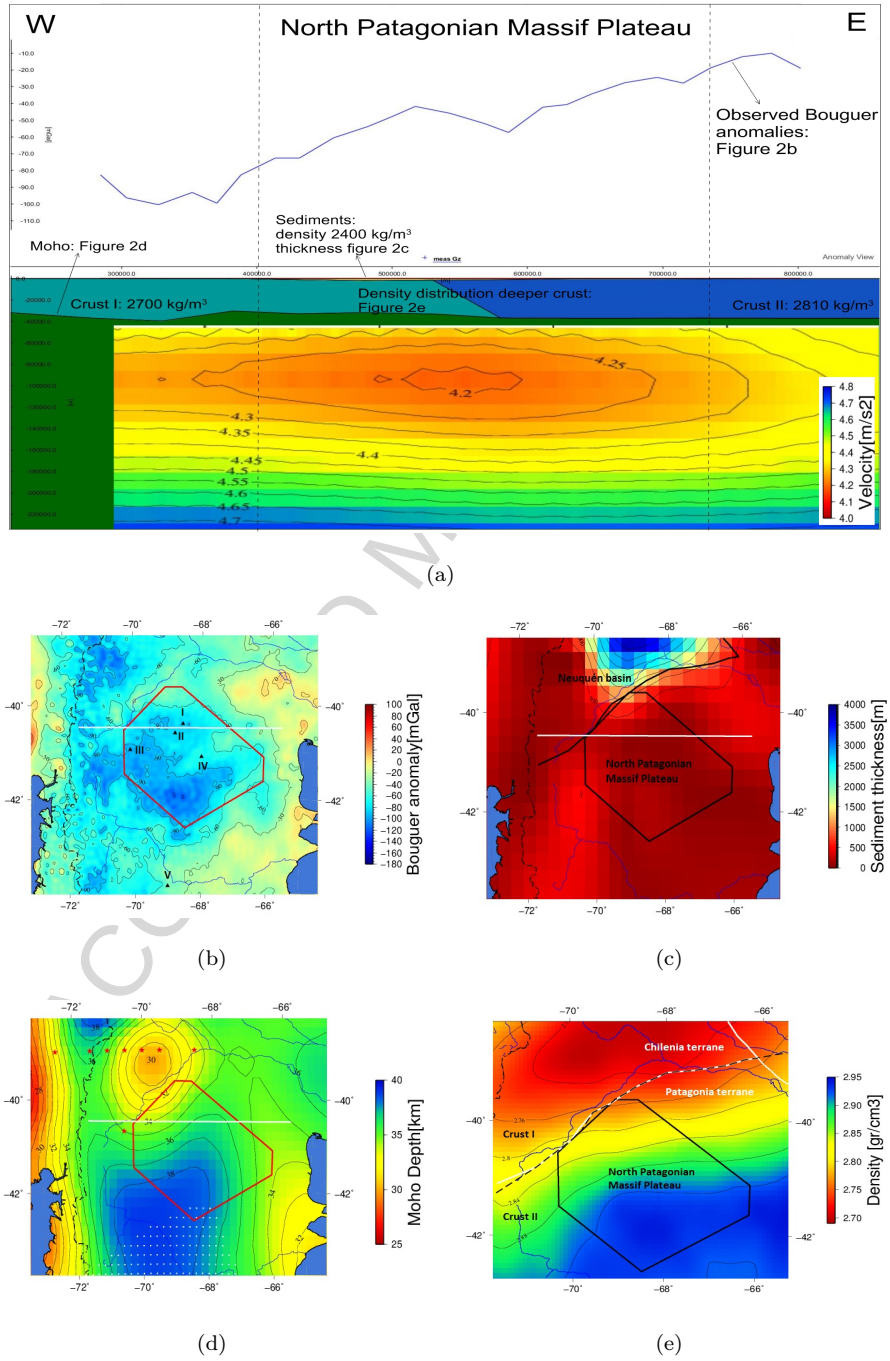

Figure 2: Initial density model. a) Schematic profile showing a cross section of the initial model and the input data. The velocity distribution profile is from SL2013Sv model (Schaeffer & Lebedev, 2013). The location of the profile is shown in white in figures 2(b), 2(c) and 2(d). b) Bouguer anomalies from EGM2008 (Pavlis et al., 2012) used as measured gravity for the 3D density model. The localities where there are xenolith data (Ponce 2016 and Mundl et al. 2015) are indicated by black triangles. I: Cerro Chenque, II: Puesto Diaz, III: Comallo, IV: Pahuaniyeu, V: Paso de Indios. c) Sediment thickness in the study area from Heine (2007). d) Moho depth of the initial model extracted from Assumpção et al. (2012). The area with white points has no resolution and was interpolated to be used in the initial model. The location of the Moho depth data from seismics are shown with red stars. e) Density configuration at 25 km depth, converted from SL2103Sv model (Schaeffer & Lebedev, 2013). The discontinuity between terranes from Chernicoff & Zappettini (2004) is shown with white solid lines. The final discontinuity between the two crustal bodies modelled is shown with black dashed line.

ACCEPTED MANUSCRIPT

and it is a global, tomographic model of the upper mantle. It was developed using surface and S-wave forms and inverted with the Automated Multimode Inversion (AMI) algorithm (Schaeffer & Lebedev, 2013). The solution was found with respect to a 3D reference model based on the model Crust 2.0 (Bassin et al., 2000) and the global velocity model ak135 (Kennett et al., 1995). The advantage of SL2013sv is that it has data coverage at every knot of the model (Schaeffer & Lebedev, 2013). The used version of the model is provided with a lateral resolution of 0.5° and a vertical resolution of 25 km.

The second model, UU-P07 (Amaru, 2007), is also a global tomographic model, but containing P-wave velocity of the crust and mantle. Its reference model is also the global velocity model ak135 (Kennett et al., 1995). It is based on a wide data set that consists of a selection of travel times from catalogs, bulletins and recordings of seismic networks and temporary experiments (Amaru, 2007). This model does not ensure data coverage in every cell of the model like the previous one.

Both tomographic models present a similar pattern of velocities. A low velocity anomaly can be seen below the NPM plateau area, between 50 and 200 km depth (Figure 2(a)). This anomaly continues to the south of the NPM but ends towards the north, where higher velocities can be observed. One of the major goals of deriving density from mantle velocity was to assess the influence of mantle anomalies (such as the one described) on the gravity field - a major requirement for inverting crustal densities using gravity (see also Klitzke et al. 2016, in press).

2.4.1. Velocity-density conversions

For the S-wave tomographic model -SL2013Sv-, two different conversions were tested and compared. The first one is based on a seismic heterogeneity ratio $R_{(\frac{\rho}{S})}$, which is a conversion factor depending on depth, whereas the second is based on the approach of Goes et al. (2000) as implemented in the computer programme of An & Shi (2007).

The density to S-wave velocity heterogeneity ratio $R_{(\frac{\rho}{S})}$ is the relation be-

ACCEPTED MANUSCRIPT

tween the lateral density perturbations relative to the spherical average ($\delta \ln(\rho)$) and the relative shear velocity perturbations ($\delta \ln(V_S)$). Revising the bibliography (Cammarano et al. 2003; Ishii & Tromp 2001; Karato & Karki 2001; Resovsky & Trampert 2003), different values for this parameter depending on depth can be found, but most of them vary between 0.15 and 0.25 for the upper mantle. The only exception is some value found for the shallow upper mantle, which is very low or negative and related to subducted slabs (Cammarano et al., 2003). $R_{(\frac{\rho}{S})}$ is mainly derived from mineral physics and is based on the assumption that the lateral variations in density are only caused by thermal variations (Ishii & Tromp, 2001). Although there may be some other sources of heterogeneity, mainly caused by compositional variations, their effect on seismic velocity is supposed to be small (less than 1% of the velocity changes, as inferred from mantle xenoliths) compared with the effect generated by thermal variations in the uppermost mantle (50 to 300 km; Goes et al. 2000; Cammarano et al. 2003).

We have converted the S-wave velocities using the vertical profile of $R_{(\frac{\rho}{S})}$ published by Simmons et al. (2009), who have determined an optimum $R_{(\frac{\rho}{S})}$ for different depth levels by testing different profiles of $R_{(\frac{\rho}{S})}$ (derived from mineralogy and considering only thermal variations) with geodynamic constraints. These authors also proposed a correction due to the temperature dependence on seismic attenuation in the upper mantle that was used in this conversion.

The second conversion applied to the S-wave velocity data was performed using "velt", a program developed by An & Shi (2007). Velt is based on the approach of Goes et al. (2000) which, in turn, assume that the upper mantle can be modelled by five basic minerals with characteristic elastic moduli. They postulate that the elastic moduli of every component of the upper mantle (M_i) is a function of the in-situ temperature (T) and pressure (P) as well as the iron content (X_{Fe}):

$$M_i(P,T,X_{Fe}) = M(P_0,T_0,X_{Fe}) + (T-T_0)\frac{\delta M}{\delta T} + (P-P_0)\frac{\delta M}{\delta P} + X_{Fe}\frac{\delta M}{\delta X_{Fe}}, \quad (4)$$

ACCEPTED MANUSCRIPT

where M_i can be either of the elastic parameters: compressibility (κ) or rigidity (μ). In the case of velt, the elastic moduli in normal conditions (P_0, T_0, X_{Fe}) and the derivatives have been obtained from laboratory experiments (An & Shi, 2007). Then, the elastic moduli of the upper-mantle material can be found as the Voigt-Reuss-Hill (VRH) average of the compounding minerals:

$$\langle M \rangle = \frac{1}{2}(M^{Voigt} + M^{Reuss}), \tag{5}$$

$$M^{Voigt} = \sum M_i \lambda_i \tag{6}$$

$$M^{Reuss} = (\sum \frac{\lambda_i}{M_i})^{-1} \tag{7}$$

where λ_i is the volumetric portion of the mineral i. According to An & Shi (2007), velt considers an off-cratonic mantle composition with 68% olivine, 18% orthopyroxene, 11% clinopyroxene, 3% garnet, 0% spinel and an iron content of 0.1 (the content of Fe is 10 % of the content of Fe +Mg).

Once the elastic moduli are obtained, the program calculates the S and P-wave velocities from:

$$V_S(P,T) = \sqrt{\frac{\langle \mu \rangle}{\langle \rho \rangle}} \tag{8}$$

$$V_P(P,T) = \sqrt{\langle \kappa \rangle + \frac{4\langle \mu \rangle}{3\langle \rho \rangle}} \tag{9}$$

and determines the density value iteratively by approaching the observed V_s or V_p. The programme also corrects the results for the effect of the anelasticity with a correction dependent on the frequency (Goes et al., 2000).

This methodology was also used to convert P-wave velocities of the model UU-P07 (Amaru, 2007) into densities.

ACCEPTED MANUSCRIPT

2.4.2. Density configuration as derived from seismic velocities

In total, three density configurations have been obtained for the area: for the S-wave velocity model SL2013sv, we have obtained configuration A by using the $R_{(\frac{\rho}{S})}$ parameter and configuration B by using the program velt. On the other hand, configuration C consists of densities as derived from P-wave velocity model UU-P07 by using the program velt. The spatial pattern of density in the three density configurations is similar, showing a low density anomaly below NPM area, but they differ significantly in absolute value. To better illustrate the general pattern of densities, but showing at the same time the difference in absolute value, Figure 3 shows different perspectives of the three configurations. Figure 3(a) shows a west-east profile crossing the NPM area (at $-41°S$) of configuration A. In this figure the mentioned anomaly can be observed below the NPM area; the difference with the surroundings can also be observed and is greater to the east than to the west. Figure 3(b) shows a south-north profile (at $-68°W$) of configuration C, where the low density anomaly can also be observed. In this case, the difference of densities between the NPM area and the surroundings can be observed towards the north of the NPM area while the anomaly follows to the south till the end of the study area. Figure 3(c) shows a map at 60 km depth of configuration B, where it is also possible to distinguish the anomaly of lower density below the NPM area.

Table 1 shows the statistics of the different density configurations to highlight their differences. The highest difference can be observed between configurations A and B -106 $\frac{kg}{m^3}$ in average and 1 $\frac{kg}{m^3}$ in standard deviation. The values of configuration C are generally between the values of configurations A and B.

2.5. Petrological constraints on the density configuration of the mantle

In the study area and its immediate surroundings, there are five localities with basalts carrying ultramafic xenoliths from the upper mantle (Figure 2(b)). To assess mantle densities, modal analysis data of more than 50 xenoliths published by Ponce (2016) and Mundl et al. (2015) have been studied. The xenoliths described by Ponce et al. (2015) and Ponce (2016) were carried by Eocene

ACCEPTED MANUSCRIPT

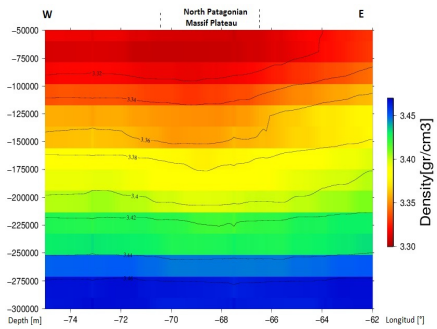

(a) W-E profile of distribution A

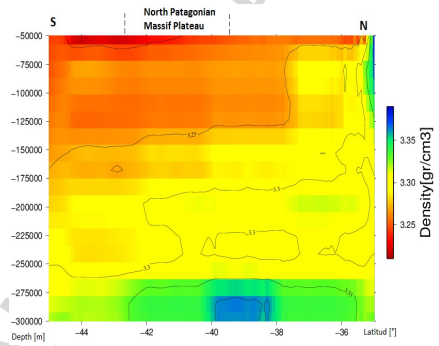

(b) S-N profile of distribution C

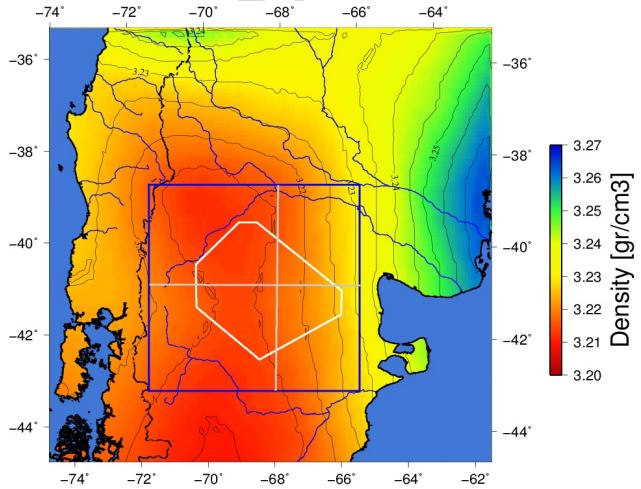

(c) 60 km depth map of distribution B

Figure 3: Density configurations for the mantle obtained from tomographic models. a) West-east profile of configuration A obtained from SL2013Sv model (Schaeffer & Lebedev, 2013) by using $R(\frac{\rho}{S})$. b) South-north profile of configuration C obtained from UU-P07 model (Amaru, 2007) using velt software (An & Shi, 2007). c) 60 km depth map of configuration B obtained from SL2013Sv model (Schaeffer & Lebedev, 2013) by using velt software (An & Shi, 2007). The location of the profiles of figures 3(a) and 3(b) are shown in grey.

ACCEPTED MANUSCRIPT

Table 1: Statistics of the different density configurations. The values are expressed in kg/m^3

Configuration	**A**	**B**	**C**
Mean	3384	3278	3288
Standard deviation	52.5	51.4	22.8
Minimum	3304	3201	3240
Maximum	3470	3379	3361

(54 Ma old) basalts of the area of Paso de los Indios (locality V, Figure 2(b)) and the xenoliths investigated by Mundl et al. (2015) were emplaced in alkali basalts of four locations within the North Patagonian Massif (Cerro Chenque, Puesto Diaz, Comallo and Prahuaniyeu; localities I, II, III and IV respectively in Figure 2(b)) during Miocene (23 Ma) to Pleistocene times (1.3 Ma). Ponce (2016) has carried out a modal analysis of the xenoliths by point counting thin section scanned images and also determined the major element chemical composition of olivine, clinopyroxene, orthopyroxene and spinel with electron microprobe analyses. Mundl et al. (2015) have also accomplished a modal analysis of xenoliths by using mass balance of whole rock and mineral compositions for some samples and point counting for others. They have also made an analysis of the mineral major element using electron microprobe analyses (Mundl et al., 2015). The xenoliths of locality V are spinel peridotites, pyroxenites, hazburguites and lherzolites (Ponce et al., 2015). In localities I, II and III, the xenoliths are mostly spinel-hazburgites and the samples from locality IV are spinel and garnet-peridotites (Mundl et al., 2015). A summary of the information about xenoliths is given in Table 2.

2.5.1. Assessment of in-situ densities from xenolith data

Hacker & Abers (2004) have developed an Excel macro to calculate physical properties of rocks for certain pressures and temperatures. One of the properties

ACCEPTED MANUSCRIPT

Table 2: Description of xenoliths in the study area

Locality	Name	Age	Composition	Method	Reference
I	Cerro Chenque	Miocene (23 Ma)	Spinel hazburguites	Modal analysis by point counting + Major element by electron microprobe	Mundl et al. (2015)
II	Puesto Diaz	Miocene (23 Ma)	Spinel hazburguites	Modal analysis by point counting + Major element by electron microprobe	Mundl et al. (2015)
III	Comallo	Pleistocene (1.3 Ma)	Spinel hazburguites	Modal analysis by point counting + Major element by electron microprobe	Mundl et al. (2015)
IV	Prahuaniyeu	Miocene (23 Ma)	Spinel and garnet peridotites	Modal analysis by point counting + Major element by electron microprobe	Mundl et al. (2015)
V	Paso de los Indios	Eocene (54 Ma)	Peridotites, piroxenites, hazburguites and Iherzolites	Modal analysis by mass balance and point counting + Major element by electron microprobe	Ponce et al. (2015); Ponce (2016)

ACCEPTED MANUSCRIPT

ACCEPTED MANUSCRIPT

that the macro is able to calculate is density, as influenced by modal or volume proportions of minerals in a sample. The first step of the density calculation is to obtain the density of every mineral composing the rock at these particular temperature and pressure conditions. Based on the density at standard temperature and pressure (ρ_0), first temperature and then pressure is interpolated (Hacker & Abers, 2004). The density ($\rho(T)$) at a given temperature T is:

$$\rho(T) = \rho_0 e^{-\phi}, \tag{10}$$

where,

$$\phi = ln(\frac{V(T)}{v_0}), \tag{11}$$

with V_0 being the molar volume at standard temperature and pressure and $V(T)$ being the molar volume at temperature T. ϕ is extracted from the variation of the expansivity with temperature that depends on a constant for each mineral (Hacker & Abers, 2004). The variation of density with pressure is given by:

$$\rho(P) = \rho_0(1 + 2f)^{2/3} \tag{12}$$

where f is the finite Eulerian strain, calculated from the pressure and the mineral properties (Hacker & Abers, 2004). Then, the density at a given temperature and pressure is calculated as:

$$\rho(T, P) = (\frac{\rho(P)}{\rho_0})\rho(T) \tag{13}$$

Once the density of every mineral is calculated, the density of the rock can be obtained by using the volume proportions of the minerals as specified in the modal analysis (Ponce, 2016; Mundl et al., 2015) and by applying:

$$\rho_{sample}(T, P) = (\sum_{i=1}^{n} \rho_i v_i)/n \tag{14}$$

ACCEPTED MANUSCRIPT

For the density calculation of the xenoliths in the study area we have used the composition derived from the modal analysis (Ponce, 2016; Mundl et al., 2015) and equilibrium temperatures and pressures. Ponce (2016) has determined these equilibrium conditions using major element analysis of clinopyroxene and orthopyroxenes cores, the two-pyroxene geo-thermometer of Brey & Köhler (1990) and the geo-barometer of clinopyroxene of Mercier (1980). The mean values of the corresponding data are 1.8 GPa for pressure and 972 $°C$ for temperature. Mundl et al. (2015) have also calculated the temperature of equilibrium using the two-pyroxene thermometer of Brey & Köhler (1990) though only by measuring the pressure in one sample. For this reason, and using the mineralogical data available in Mundl et al. (2015), we have calculated the equilibrium pressure for the xenoliths inside the NPM plateau area by using a geo-barometer of clinopyroxene of Mercier (1980). For every locality, the mean value of temperature and pressure (Figure 4) has been selected to calculate the density.

The calculated densities of xenoliths in the localities inside the NPM plateau (localities I, II, III and IV) area are illustrated in Figure 4(a) and the ones in locality V, towards the south of the NPM plateau, are shown in the histogram of Figure 4(b). In Figure 4(c) all the samples of the localities inside the NPM are shown together. The densities shown in Figure 4 and calculated considering xenolith data are compared with the ones obtained by converting seismic velocities. Therefore, the density values of the configurations A, B and C (Figure 3) in the localities I, II, III and IV and at corresponding P conditions have been obtained and shown in the histograms of Figure 4. The density configuration (obtained from seismic velocities) that best fits with the densities determined by xenoliths is configuration C (configuration of densities obtained from P-wave velocities). That is why, we have chosen configuration (C) to integrate the initial density model.

ACCEPTED MANUSCRIPT

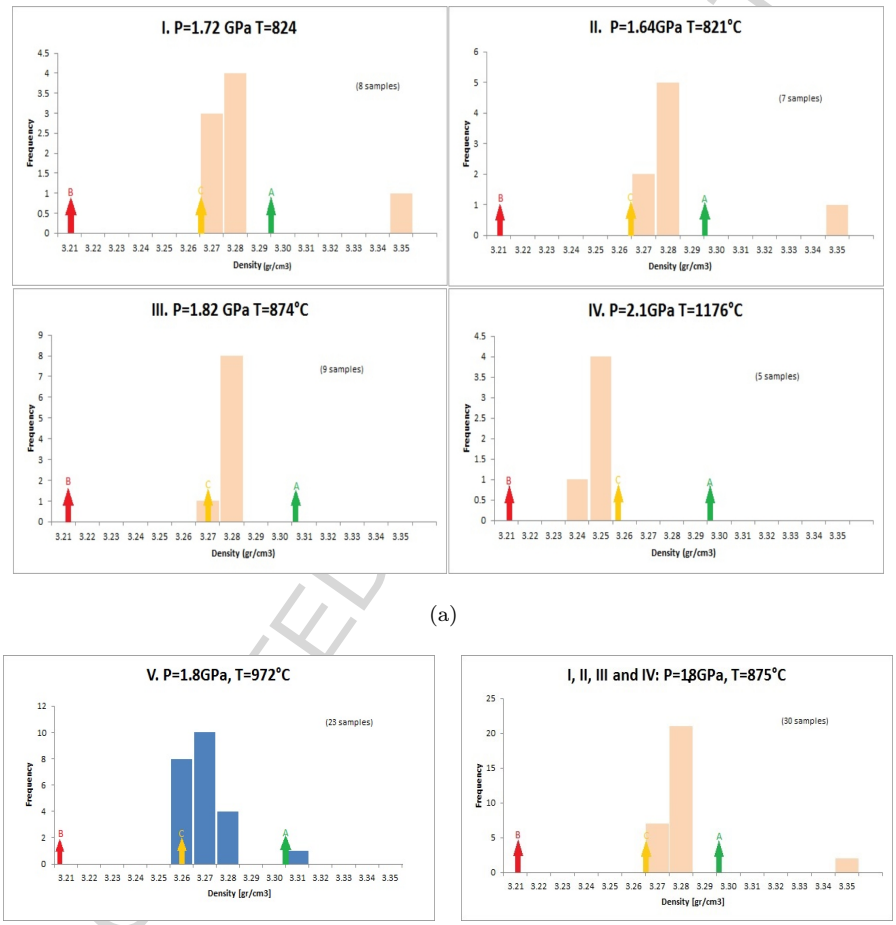

Figure 4: Histograms containing the density calculated for xenolith samples (data from Ponce 2016 and Mundl et al. 2015) at mantle pressures and temperatures and a comparison with density configurations from tomographic models. The arrows show the densities of the different configurations (A, B and C) in the localities where the xenolith samples were found, at a depth equivalent to the equilibrium pressure (considering lithostatic pressure, using ak135 pressures; Kennett et al. 1995) a) Histograms with density values of xenoliths inside the NPM plateau area, specified by locality. b) Histogram with density values of Paso de los Indios (locality V) towards the south of the NPM plateau area. c) Histogram with density values of all xenolith samples inside the NPM plateau area (localities I, II, III, IV and V).

ACCEPTED MANUSCRIPT

3. 3D Gravity modelling procedure and results

3.1. Initial 3D density model

The initial density model (illustrated in Figure 2) is composed by:

- the sediment thickness from ICONS Atlas (Heine 2007; Figure 2(c))
- the sediment density assumed to be a constant according to the lithologies of Neuquén basin (Figure 2(a))
- the Moho depth from Assumpção et al. (2012) (Figure 2(d))
- the density of the two cristalline crust domains from a combination of surface geology and the density configuration at 25 km obtained from the conversion of the S-wave velocities of Schaeffer & Lebedev (2013) (Figures 2(a) and 2(e))
- the mantle density configuration from P-wave velocities of model UU-P07 (Amaru 2007; configuration C).

This initial density model generates a gravity residual (measured minus calculated anomalies) that is illustrated in Figure 5. As can be observed, the calculated anomalies fit well with the measured ones at the points where the initial Moho is constrained -residual gravity of < 30 $mGal$ in absolute value. A negative residual, reaching -100 $mGal$, can be clearly observed in the NPM plateau area (Figure 5) and indicates a mass excess in the model. Other residuals can be observed on the map of Figure 5 and they are located near the discontinuities between terranes.

3.2. Final 3D density model

The modelling process was conducted by shifting the free parameter (the Moho depth) to greater depths in the NPM area to fit the gravity. It was modified at every point except where Assumpção et al. (2012) Moho is constrained by seismic data (Figure 2(d)). The resulting Moho can be observed in Figure 6(a) and the residuals of the gravity in Figure 6(b). According to the improved

ACCEPTED MANUSCRIPT

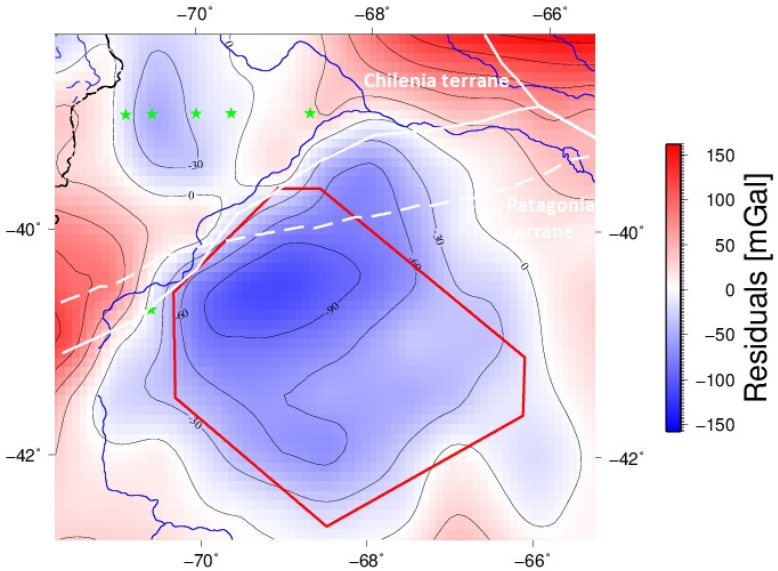

Figure 5: Gravity residuals of the initial model. The location of the constraining independent Moho depth data is shown with green stars. The discontinuity between terranes from Chernicoff & Zappettini (2004) is shown with white solid lines, and the S-wave velocity constrained boundary between terranes in a white dash line.

ACCEPTED MANUSCRIPT

Table 3: Statistics of the residuals of the final model. The values are expressed in $mGal$

Entire study area				**At points where the Moho is constrained by seismic data**	
Mean	**Standard deviation**	**Maximum value**	**Minimum value**	**Mean**	**Maximum**
$-7.76e^{-8}$	27.05	57.81	-59.83	14.95	25.68

gravity-constrained model, the crust is thicker in the NPM plateau area than in its surroundings (Figure 6(a)). It varies between 40 and 50 km, increasing from the borders of the plateau to a point near the center of the massif and it has an elongated shape in north-east to south-west direction (Figure 6(a)). The greater difference between the NPM and the surroundings is observed towards the north, where the Neuquén basin is located and the shallowest Moho depths of the modelled area can be observed. The lowest difference is observed towards the west of the NPM plateau area, where the compressional forces of the subduction margin have caused a thickening of the crust. In the north-west corner of the modelled area, the southern extreme of the Andes crustal root can be observed (Figure 6(a)). Interestingly, the Moho depths inside the NPM area are similar to the depths found in mountain crustal roots.

The residual map of Figure 6(b) shows a similar pattern in the northern part (Chilenia terrane) to the residuals of the initial model but with lower values. In the southern part of the model (Patagonia terrane), the long wave-length anomaly observed in Figure 5 was eliminated considering the observed gravity and a smaller residual anomaly can be observed. The statistics of the residuals can be observed in Table 3. In the locality where there are young xenoliths (locality III; Figure 6(b)) a negative residual is observed, indicating that there is a mass excess in the model. However, the localities with older xenoliths are outside the negative residuals.

ACCEPTED MANUSCRIPT

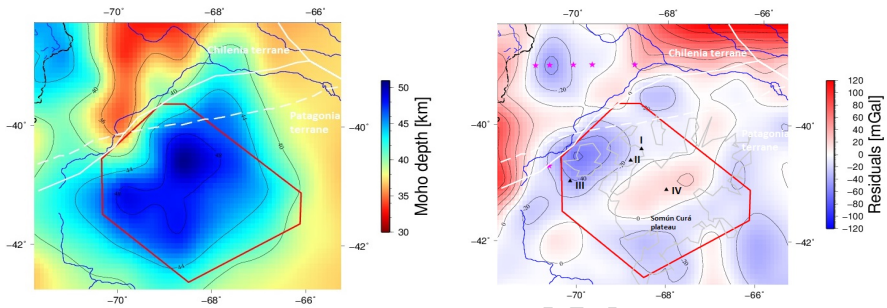

(a) (b)

Figure 6: Moho and residuals of the final model. The discontinuity between terranes from Chernicoff & Zappettini (2004) is shown with white solid lines and the discontinuity in the velocity distribution with a dash line. a) Resulting Moho depth. b) Gravity residuals of the resulting model. The location of the constraining independent Moho depth data is shown with red stars. The outcropping basalts of the area are delimited in grey. The location of the xenolith samples are shown with black triangles.

4. Discussion

The setup of the initial 3D density model has involved some important assumptions. Concerning sediments, we have selected a density value that considers, intrinsically, a certain porosity for the given lithology. If this assumption is changed between the possible extremes, i.e. totally compacted sediments without porosity or unconsolidated sediments (of 70 % porosity), the mean of the residuals (Table 3) almost remain the same but the standard deviation slightly increase (in the first case by 2 $mGal$ and in the second by 7 $mGal$). Therefore, the density value chosen for the sediments does not significantly affect the main modelling results (i.e. crustal thickness). Moreover, in most of the study area the pattern of the residuals is preserved in spite of the changes in the sediment density. We conclude that the density of the sedimentary unit does not significantly affect the main results of the modelling procedure (i.e. the depth distribution of the Moho).

Another important predefined feature of the model is the mantle density configuration. If this configuration is changed in the final model, the residu-

ACCEPTED MANUSCRIPT

als increase significantly as can be observed in Table 4. This table shows the statistics of the residuals if configuration A, B or a constant mantle density replaces the mantle density configuration of the final model. All the statistical parameters of the residuals (standard deviation, minimum and maximum values) substantially increase for other configurations (table 4) compared with the configuration of the final model (table 3). The same can be observed in the residuals at points where the Moho is constrained by seismic data (tables 3 and 4). Therefore, the selection of the mantle density configuration is very important in the modelling process and has a large impact on the results.

The selection of the mantle density configuration for the final model was based on the comparison of every derived configuration with determinations of density from independent xenolith data. This procedure ensures the reliability of our choice, since it was based on independent data that validate the conversion. The selected configuration is derived from P-wave velocities and the reason why it gave the best result may come from several causes. One of the reasons could be the type of wave, as the P waves are less dependent to anisotropy or maybe the conversion employed, because we made two conversions with S-wave data that gave different results and thus it can be that none of them are appropriate in this case. Other reason can be the resolution, as the S-wave model cannot resolve the subducting plate at the model latitude, thus maybe the resolution is not enough in the modeled area.

4.1. Implications of the modelled crustal configuration

There is an important difference between the modelled crust-mantle discontinuity (Figure 6(a)) and the initial Moho (Assumpção et al. 2012; Figure 2(d)) in the areas where this model has no independent constraints. The most remarkable difference is that the resulting Moho distinguishes the NPM as an area of increased crustal thickness compared to the surroundings. According to the model, the Moho inside the NPM plateau has a mean depth of 45.6 km and a standard deviation of 2.7 km (Figure 6(a)) and an important difference of depth, of between 2 and 7 km, with respect to the surroundings, allowing

ACCEPTED MANUSCRIPT

Table 4: Statistics of the residuals of models with different mantle density configurations. The residuals are calculated for models that integrate the Moho of the final model. The values are expressed in *mGal*

Residuals	**With configuration A**	**With configuration B**	**With constant mantle density**
Average	$1.82e^{-7}$	$6.36e^{-8}$	$3.54e^{-7}$
Standard deviation	54.17	55.16	52.46
Maximum value	119.72	119.27	134.35
Minimum value	-99.95	-102.38	-86.17
Mean of the values at Moho constraining points	33.55	45.99	37.81
Maximum of the values at Moho constraining points	51.66	64.19	56.48

ACCEPTED MANUSCRIPT

ACCEPTED MANUSCRIPT

us to distinguish the NPM plateau on the Moho map (Figure 6(a)). An evident correlation can be observed between the described Moho shape and the topography that also distinguishes the area as a plateau (Figure 1). As isostasy assumes equal loads at a certain depth of compensation, the relation between deep Moho and high topography in the area could indicate that it is in isostatic equilibrium at crustal scale, i.e. the great depth of the Moho is compensated by a high topography to equal the loads at a crustal scale. This would have contributed to the present-day elevation of the NPM plateau and would also indicate that the isostatic forces may have played a role during the Paleogene uplift. The recent work of Álvarez Pontoriero et al. (2016) also suggests that the NPM plateau area would be in isostatically compensated.

Concerning the modelling of crustal densities, we have used the 25 km depth velocity distribution of Schaeffer & Lebedev (2013) tomographic model where an S-wave velocity trend, increasing from north-west to south-east, can be seen (Figure 2(e)). Searching for geological evidence that could explain such a difference in velocities, we found that the trend fits with the sutures of the paleozoic terranes proposed by Ramos (1988). We have converted the velocities into densities for this depth and tested them against gravity to validate the densities found. As a result, two different density domains were modelled having an important density contrast of 110 $\frac{kg}{m^3}$ (Chilenia has a lower crustal density than Patagonia; Figure 2(a)). In the correlation between the velocity trend and the different terranes it is possible to observe that the present-day configuration of the crust traces back to Paleozoic times. It can be inferred from the model that the two mentioned terranes are very different in composition, which supports the idea of their different origins (Ramos, 1988; Gonzalez et al., 2010, 2011a,b). In conclusion, the difference in mean crustal density between both terranes would be related with their different origins and compositions.

The surface boundary between terranes is located to the north of the depth-integrated boundary constrained by S-wave velocity (Figure 5); this could indicate that the boundary dips to the south coinciding with the hypothesis of Ramos (1988) that Patagonia collided Gondwana generating a subduction dip-

ACCEPTED MANUSCRIPT

ping south-west beneath the NPM. This posible tectonic scenario would also be related with the shape of the Moho in the NPM area which is thickened in a SW-NE direction following the sutures between terranes. The thickening in this direction may have a relation with the collision of both terranes. There are residuals in the area between the surface expression of the sutures between terranes and the plotted contour levels of the density at 25 km depth (Figure 5). They can be caused by the difference between the modelled limit between crustal bodies (following the surface sutures) and the real one, with its continuation in depth that is unknown.

After modelling, there are still gravity residuals (Figure 6(b)) that, due to their wavelength - 100 to 200 km -, seem to be caused by density heterogeneities inside the crust. Moreover, in some points inside the NPM plateau area there are spatial correlation between the residuals and basaltic plateaus, such us the biggest residual of the area (in absolute value) that coincides with one of the basaltic plateau (north-west of the NPM; Figure 6(b)). This basaltic plateau is also near locality III (Figure 6(b)), where the youngest xenoliths are, and therefore the negative residual can be caused by a decrease in density related with magmatic events (thermal effect that decreased the density). In this context, it can be assumed that the magmatism present in the area could have differentiated the crust generating the observed crustal heterogeneities.

4.2. Geodynamic hypothesis

The thickened crust beneath the North Patagonian Massif plateau has an origin difficult to track. This region of Gondwana was subject to strike-slip motion of terranes in the early Paleozoic (Gonzalez et al. 2010, 2011a and Gonzalez et al. 2011b). In the late Paleozoic there was granitic plutons emplacement in the region (Aragón et al., 2010) that were exhumated and eroded since the Triassic to the Cretaceous to yield the Gondwana planation surface (Aragón et al., 2010), preserved in the NPM plateau to the present time. In mid Jurassic time, the region was affected by the breakup of Gondwana by a major thermal anomaly, that gave rise to the Atlantic ocean. We suggest that the Moho of

ACCEPTED MANUSCRIPT

the region, at the uplift moment (Paleogene), was modelled for the described processes: the forces involved in the amalgamation of the terranes, the possible orogeny that generates the granitic emplacement and the thermal anomaly of the breakup of Gondwana.

During the Paleogene there was a plate rearrangement that led to a thermal discontinuity in the mantle below the NPM. Several papers refer the mentioned discontinuity but with different hypothesis and explanations. Kay et al. (1993, 2007) proposed the existence of a transient hot spot in the area, Muñoz et al. (2000), a corner flow due to a slab roll back, De Ignacio et al. (2001) a shallow mantle uplift caused by a corner flow and Aragón et al. (2011 b, 2015) an astenospheric window generated by the detachment of the Aluk plate during the subduction of Farallon-Aluk ridge. In this period when the area were subjected to an extensional regime, the heating of the mantle would have led to a decrease in the density which, together with the thicker crust of the NPM plateau, would have generated the isostatic disequilibrium and the consequent uplift. This regional uplift of the plateau was controlled by four major lineaments of remnant fault systems that in the Paleogene extensional regime allowed normal fault displacement.

Nowadays, the reasons for the NPM to preserve its high elevation would be the apparent isostatic balance, as can be observed in the developed model, together with the possible low density and/or partial melt that can be suppose in the low velocities observed in the mantle. The present compression derived from the subduction in the west margin of South America (from Miocene on) can be also contributing to preserve the elevation of the area and may affect the present thickness of the crust.

5. Conclusions

With the aim of obtaining the crustal configuration of the NPM, as a key to understand its present-day isostatic state, we developed a lithospheric-scale 3D gravity modelling of the area. Since there is no seismic information about

ACCEPTED MANUSCRIPT

the crust, we needed to assess the mantle density contribution to the observed gravity field to constrain the model. This was done by combining seismological and xenolith data. The main modelling result is the Moho depth configuration that is consistent with multi-disciplinary data.

The modelled Moho has a depth of 46 ± 3 km in the NPM plateau area and presents a difference of 2 to 7 km with respect to its surroundings. The large depth of the Moho correlates with the high topography of the NPM which is indicative of isostatic equilibrium in a crustal scale. This isostatic equilibrium may be a contribution to the present high topography of the NPM plateau and together with a possible high temperature and the active tectonics in the west margin would keep the study area elevated. Moreover, the thicker crust of the NPM plateau and its present isostatic compensation would indicate that the isostasy would have had some influence in the sudden uplift occurred in the Paleogene related with the isostatic disequilibrium generated by the thermal anomaly referred by several authors (Aragón et al., 2011 b, 2015; Kay et al., 1993, 2007; Muñoz et al., 2000; De Ignacio et al., 2001) .

In the shape of the Moho, a NE-SW striking domain of large crustal thickness can be distinguished within the NPM. It correlates with the strike direction of the proposed suture between ancient crustal terranes and thus might have some relation with the Paleozoic amalgamation of Gondwana.

The 3D density model integrates a density contrast within the crust that has been derived from crustal S-wave velocities and correlates quite well with the proposed Paleozoic suture zone between Patagonia and Chilenia (Chernicoff & Zappettini, 2004; Ramos, 1988).

Further density discontinuities within the crust are indicated by the final residual between modelled and measured gravity. The consistency of the main residuals inside NPM area with volcanic areas points to a magmatically differentiated crust. Nevertheless, more data is required to analyse these smaller wavelength discontinuities.

ACCEPTED MANUSCRIPT

References

Alvarado, P., Beck, S., & Zandt, G. (2007). Crustal structure of the south-central andes cordillera and backarc region from regional waveform modelling. *Geophysics Journal International*, *170*, 858–875. doi:10.1111/j.1365-246X.2007.03452.x.

Álvarez Pontoriero, O., Klinger, F. L., Gimenez, M., Ruiz, F., & Martinez, P. (2016). Density and thermal structure of the southern andes and adjacent foreland from 32 to 55 s using earth gravity field models. In *Growth of the Southern Andes* (pp. 9–31). Springer.

Amaru, M. (2007). *Global travel time tomography with 3-D reference models*. Ph.D. thesis Faculty of Geosciences Utrecht University.

An, M., & Shi, Y. (2007). Three-dimensional thermal structure of the chinese continental crust and upper mantle. *Science in China Series D: Earth Sciences*, *50*, 1441–1451.

Aragón, E., Aguilera, Y., Cavarozzi, C. E., & Ribot, A. (2010). The north patagonian altiplano and the somún curá basaltic plateau. *Geociencias*, *29*, 527–532.

Aragón, E., Brunelli, D., Castro, A., Rivalenti, G., Varela, R., Rabbia, O., Spackman, W., Cavarozzi, C. E., Aguilera, Y., Ribot, A., Mazzucchelli, M., D'Eramo, F., & Demartis., M. L. (2011 b). Tectono-magmatic response to major convergence changes in the north patagonian suprasubduction system: The paleogene subduction-transcurrent plate margin transition. *Tectonophysics.*, *509*, 218–237. doi:10.1016/j.tecto.2011.06.012.

Aragón, E., D' Eramo, F., Pinotti, L., Aguilera, Y., Cavarozzi, C., Demartis, M., Gómez Dacal, M. L., Hernando, I., & Fuentes, T. (2015). Un rift pasivo durante el paleógeno en patagonia septentrional: Evolución y cambios de estilo extensional. XIV congreso geológico chileno. In *XIV Congreso Geológico Chileno*.

ACCEPTED MANUSCRIPT

Aragón, E., Tassara, A., Tocho, C., Mendoza, L. P. M., Spackman, W., Rabbia, O., Perdomo, R., & Bertotto., W. G. (2011 a). Upper mantle geodynamic constrains beneath the north patagonian massif, argentina. In *18º Congreso Geológico Argentino* (pp. 350–351).

Assumpção, M., Feng, M., Tassara, A., & Julià, J. (2012). Models of crustal thickness for south america from seismic refraction, receiver functions and surface wave tomography. *Tectonophysics*, (pp. –). URL: `http://www.sciencedirect.com/science/article/pii/S0040195112007330`. doi:http://dx.doi.org/10.1016/j.tecto.2012.11.014.

Bassin, C., Laske, G., & Masters, G. (2000). The current limits of resolution for surface wave tomography in north america. In *EOS Trans AGU* (p. F897). volume 81.

Birch, F. (1961). The velocity of compressional waves in rocks at 10 kilobars, part 2. *Journal of Geophysical Research*, *66 (7)*, 2199–2224.

Brey, G. P., & Köhler, T. (1990). Geothermobarometry in fourphase lherzolites ii. new thermobarometers and practical assessment of existing thermobarometers. *Journal of Petrology*, *31*, 1353–1378.

Cammarano, F., Goes, S., Vacher, P., & Giardini, D. (2003). Inferring upper-mantle temperatures from seismic velocities. *Physics of the Earth and Planetary Interiors*, *138*, 197–222.

Canale, N., Ponce, J. J., Carmona, N. B., Drittanti, D. I., Olivera, D. E., Martinez, M. A., & Bournod, C. N. (2015). Sedimentología e icnología de deltas fluvio-dominados afectados por descargas hiperpícnicas de la formación lajas (jurásico medio), cuenca neuquina, argentina. *Andean Geology*, *42(1)*, 114–138.

Castro, A., Aragón, E., Díaz-Alvarado, J., Blanco, I., García-Casco, A., Vogt, K., & Liuf, D.-Y. (2011). Age and composition of granulite xenoliths from

ACCEPTED MANUSCRIPT

paso de indios, chubut province, argentina. *Journal of South American Earth Sciences.*, . doi:http://dx.doi.org/10.1016/j.jsames.2011.06.001.

Chernicoff, C. J., & Zappettini, E. O. (2004). Geophysical evidence for terrane boundaries in south-central argentina. *Gondwana Research*, *7(4)*.

De Ignacio, C., López, I., Oyarzún, R., & Marquez, A. (2001). The northern patagonia somuncura plateau basalts: a product of slabinduced, shallow asthenospheric upwelling? *Terra Nova*, *13*, 117–121.

Goes, S., Govers, R., & Vacher, P. (2000). Shallow mantle temperatures under europe from P and S wave tomography. *Journal of Geophysical Research*, *105*, 153–169.

Gonzalez, P. D., Sato, A. M., Naipauer, M., Varela, R., Llambias, E., Basei, E., Sato, K., & Sproesser, W. (2011b). Does patagonia represent a missing piece detached from the ross orogen? *East meet West: Abstracts, Rio de Janeiro, Brasil, 1p.*, .

Gonzalez, P. D., Sato, A. M., Naipauer, M., Varela, R., Llambias, E., Greco, G., Gonzalez, S., & Garcia, V. (2011a). Conexión macizo norpatagónico - antártida oriental: Fósiles arqueociátidos, comparación geológica y circones detríticos. *18° Congreso Geológico Argentino. Neuquén*, (pp. 87–88).

Gonzalez, P. D., Varela, R., Sato, A. M., Greco, G., Naipauer, M., & Llambias, E. (2010). Evidencias geológicas y paleontológicas en la formación el jagüelito para la conexión patagonia-antártida durante el paleozoico inferior. *10º Congreso Argentino de Paleontología y Bioestratigrafía y 7º Congreso Latinoamericano de Palelontología. La Plata, Buenos Aires*, (p. 48).

Gregori, D. A., Kostadinoff, J., Strazzere, L., & Raniolo, A. (2008). Tectonic significance and consequences of the gondwanide orogeny in northern patagonia, argentina. *Gondwana Reasearch*, . doi:10.1016/j.gr.2008.04.005.

ACCEPTED MANUSCRIPT

Götze, H. J., & Schmidt, S. (2010). Igmas+: a new 3D gravity, FTG and magnetic modeling software tool. *Expanded abstracts from the ASEG-PESA Airborne Gravity 2010 Workshop*, (pp. 91–96).

Hacker, B. R., & Abers, G. A. (2004). Subduction factory 3: An excel worksheet and macro for calculating the densities, seismic wave speeds, and h2o contents of minerals and rocks at pressure and temperature. *Geochemistry, Geophysics, Geosystems*, *5 (1)*. doi:10.1029/2003GC000614.

Heine, C. (2007). *Formation and Evolution of intracontinental basins*. Ph.D. thesis School of Geosciences, The University of Sydney, Australia.

Ishii, M., & Tromp, J. (2001). Even-degree lateral variations in the earth's mantle constrained by free oscillations and the free-air gravity anomaly. *Geophys. J. Int.*, *145*, 77–96.

Johannsen, A. (1931). *Descriptive Petrography of the Igeous Rocks*. University of Chicago Press.

Julià, J., & Mejía, J. (2004). Thickness and vp/vs ratio variation in the iberian crust. *Geophysics Journal International*, *156*, 59–72. doi:0.1111/j.1365-246X.2004.02127.x.

Karato, S., & Karki, B. (2001). Origin of lateral variation of seismic wave velocities and density in the deep mantle. *Geophys. J. Int.*, *106 NO.B10*, 21771–21783.

Kay, S. M., Ardolino, A. A., Franchi, M., & Ramos, V. A. (1993). Origen de la meseta de somún curá: distribución y geoquímica de sus rocas volcánicas máficas. *XII Congreso Geológico Argentino*, *4*, 236–248.

Kay, S. M., Ardolino, A. A., Gorring, M. L., & Ramos, V. A. (2007). The somuncura large igneous province in patagonia: Interaction of a transient mantle thermal anomaly with a subducting slab. *Journal of Petrology*, *48*, 43–77. doi:10.1093/petrology/egl053.

ACCEPTED MANUSCRIPT

Kennett, B. L. N., Engdahl, E. R., & Bulland, R. (1995). Constraints on seismic velocities in the earth from traveltimes. *Geophys. J. Int.*, *122 (1)*, 108–124.

Klitzke, P., Sippel, J., Faleide, J. I., & Scheck-Wenderoth, M. (2016, in press). A 3d gravity and thermal model for the barents sea and kara sea. *Tectonophysics*, .

Kostadinoff, J., Gregori, D., & Raniolo, A. (2005). Configuración geofísica-geológica del sector norte de la provincia de río negro. *Revista de la Asociación Geológica Argentina*, *60 (2)*, 368–376.

Lowrie, W. (2007). *Fundamentals of Geophysics*. Cambridge University Press. doi:http://dx.doi.org/10.1017/CBO9780511807107.

Mercier, J. C. C. (1980). Single-pyroxene thermobarometry. *Tectonophysics*, *70*, 1–37.

Mundl, A., Ntaflos, T., Ackerman, L., Bizimis, M., Bjerg, B. A., Wegner, W., & Hauzenberger, C. A. (2015). Geochemical and os–hf–nd–sr isotopic characterization of north patagonian mantle xenoliths: Implications for extensive melt extraction and percolation processes. *Journal of Petrology*, (pp. 1–31). doi:10.1093/petrology/egv048.

Muñoz, J., Troncoso, R., Duhart, P., Crignola, P., Farmer, L., & Stern, C. R. (2000). The relation of the mid-tertiary coastal magmatic belt in south–central chile to the late oligocene increase in plate convergence rate. *Revista Geológica de Chile*, *27*, 177–203.

Nakajima, J., Matsuzawa, T., Hasegawa, A., & Zhao, D. (2001). Three-dimensional structure of vs, vp and vp/vs beneath northeastern japan: Implications for arc magmatism and fluids. *Journal of Geophysical Research*, *106*, 843–857.

Pankhurst, R. J., Rapela, C. W., Fanning, C. M., & Marquez, M. (2006). Gondwanide continental collision and the origin of patagonia. *Herat Science Reviews*, *76*, 235–257.

ACCEPTED MANUSCRIPT

Pavlis, N. K., Holmes, S. A., Kenyon, S. C., & Factor, J. K. (2012). The development and evaluation of the earth gravitational model 2008 (egm2008). *J. Geophys. Res.*, *117*. doi:http://dx.doi.org/10.1029/2011JB008916.

Ponce, A. D. (2016). *Petrología de los xenolitos del manto alojados en rocas basálticas del Paleoceno-Eoceno en la zona de Paso de Indios, provincia del Chubut*. Ph.D. thesis Facultad de Ciencias Naturales y Museo, Universidad Nacional de La Plata.

Ponce, A. D., Bertotto, G. W., Zanetti, A., Brunelli, D., Giovanardi, T., Aragón, E., Bernardi, M. I., Hémond, C., & Mazzucchelli, M. (2015). Short-scale variability of the sclm beneath the extra-andean back-arc (paso de indios, argentina): Evidence from spinel-facies mantle xenoliths. *Open Geosciences. De Gruyter open*, *7*, 362–385.

Ramos, V. A. (1988). Tectonics of the late proterozoic–early paleozoic: a collisional history of southern south america. *Episodes*, *11*, 168–174.

Ramos, V. A. (1994). Terranes of southern gondwanaland and their control in the andean structure (30–33 s latitude). In *Tectonics of the Southern Central Andes* (pp. 249–261). Springer.

Rapela, C. W., Pankhurst, R. J., Fanning, C. M., & Herve, F. (2005). Pacific subduction coeval with the karoo mantle plume: the early jurassic subcordilleran belt of northwestern patagonia. *Terrane Processes at the Margins of Gondwana. Geological Society of London, Special Publications,*, *246*, 217–239.

Resovsky, J., & Trampert, J. (2003). Using probabilistic seismic tomography to test mantle velocity-density relationships. *Earth and Planetary Science Letters*, *215*, 121–134. doi:10.1016/S0012-821X(03)00436-9.

Schaeffer, A. J., & Lebedev, S. (2013). Global shear-speed structure of the upper mantle and transition zone. *Geophys. J. Int.*, *194 (1)*, 417–449. doi:10.1093/gji/ggt095.

ACCEPTED MANUSCRIPT

Simmons, N. A., Forte, A. M., & Grand, S. P. (2009). Joint seismic, geodynamic and mineral physical constraints on three-dimensional mantle heterogeneity: Implications for the relative importance of thermal versus compositional heterogeneity. *Geophys. J. Int.*, *177*, 1284–1304. doi:10.1111/j.1365-246X.2009.04133.x.

Tassara, A., & Echaurren, A. (2012). Anatomy of the chilean subduction zone: Three-dimensional density model upgraded and compared against global-scale models. *Geophysical Journal International*, . doi:10.1111/j.1365-246X.2012.05397.x.

Vaughan, A. P. M., & Pankhurst, R. J. (2008). Tectonic overview of the west gondwana margin. *Gondwana Research*, *13*, 150–162.

ACCEPTED MANUSCRIPT

ACCEPTED MANUSCRIPT

Highlights

- A lithospheric 3D density model was developed for the North Patagonian Massif area.
- Mantle density configuration obtained through seismological and xenoliths data.
- Correlation between crustal density contrasts in the model with Paleozoic terranes.
- Modelled Moho depth below North Patagonian Massif plateau deeper than surroundings.

ACCEPTED MANUSCRIPT